Chiral nematic nanocomposites with pitch gradient elaborated by filtration and ultraviolet curing of cellulose nanocrystal suspensions

S. Mandin, L. Metilli, M. Karrouch, C. Lancelon-Pin, J.-L. Putaux, W. Chèvremont, E. Paineau, N. Hengl, B. Jean, F. Pignon

Carbohydrate Polymers 337 (2024) 122162

Contents lists available at ScienceDirect

Carbohydrate Polymers

journal homepage: www.elsevier.com/locate/carbpol

Chiral nematic nanocomposites with pitch gradient elaborated by filtration and ultraviolet curing of cellulose nanocrystal suspensions

S. Mandin [a], L. Metilli [b], M. Karrouch [a], C. Lancelon-Pin [b], J.-L. Putaux [b], W. Chèvremont [c], E. Paineau [d], N. Hengl [a], B. Jean [b], F. Pignon [a,*]

[a] Univ. Grenoble Alpes, CNRS, Grenoble INP (Institute of Engineering Univ. Grenoble Alpes), LRP, F-38000 Grenoble, France
[b] Univ. Grenoble Alpes, CNRS, CERMAV, F-38000 Grenoble, France
[c] ESRF, The European Synchrotron, CS 40220, F-38043 Grenoble Cedex 9, France
[d] Université Paris Saclay, CNRS, Laboratoire de Physique des Solides, 91405 Orsay Cedex, France

ARTICLE INFO

Keywords:
Cellulose nanocrystal (CNC)
Nanocomposite
Filtration
UV-curing
Cholesteric structure
Pitch gradient

ABSTRACT

An innovative method combining frontal filtration with ultraviolet (UV) curing has been implemented to design cellulosic nanocomposite films with controlled anisotropic textures from nanometric to micrometric length scales. Namely, an aqueous suspension containing poly (ethylene glycol) diacrylate polymer (PEGDA) as a photocurable polymer and cellulose nanocrystals (CNCs) at a 70/30 mass ratio was processed by frontal filtration, followed by *in-situ* UV-curing in a dedicated cell. This procedure allowed designing nanocomposite films with highly oriented and densely-packed CNCs, homogeneously distributed in a PEGDA matrix over a thickness of *ca.* 500 μm. The nanocomposite films were investigated with small-angle X-ray scattering (SAXS), by raster-scanning along their height with a 25 μm vertically-collimated X-ray beam. The CNCs exhibited a high degree of orientation, with their director aligned parallel to the membrane surface, combined with an increase in the degree of alignment as concentration increased towards the membrane surface. Scanning electron microscopy images of fractured films showed the presence of regularly spaced bands lying perpendicular to the applied transmembrane pressure, highlighting the presence of a chiral nematic (cholesteric) organization of the CNCs with a pitch gradient that increased from the membrane surface to the bulk.

1. Introduction

Biosourced and biodegradable materials constitute a potential solution to limit the environmental impact of petrosourced materials. As a result, many studies are focusing on the use of cellulose, the basic structural unit in plants, marine animals (tunicates), algae, certain species of fungi, and some bacteria (Nechyporchuk et al., 2016). So-called nanocelluloses can be extracted from these sources in the form of cellulose nanofibers (CNFs) and nanocrystals (CNCs), and bacterial cellulose (BC).

CNCs are rodlike particles with a width D of 3 to 20 nm and a length L from 100 nm to several microns, depending on the source and production conditions, *i.e.* displaying an aspect ratio (L/D) of 10 to 100. The general fabrication protocol involves sulfuric acid hydrolysis of cellulose fibers, which digest their disorganized domains while leaving the crystalline particles intact. The sulfuric acid treatment results in the formation of hemisulfate groups on the CNC surface, endowing the particles with negative charge and colloidal stability in aqueous suspensions from electrostatic repulsion (Marchessault et al., 1959). CNC suspensions exhibit a liquid-crystalline behavior in water, as also observed for other rodlike particles such as vanadium pentoxide (Zocher, 1925), metal oxide nanoparticles (Davidson et al., 1994; Davidson & Gabriel, 2005; Lekkerkerker & Vroege, 2013), poly(tetrafluoroethylene) whiskers (Folda et al., 1988), Tobacco mosaic virus (TMV) (Bawden et al., 1936), filamentous bacteriophage *fd* virus (Dogic & Fraden, 2000; Grelet & Fraden, 2003), DNA fragments (Strzelecka et al., 1988), collagen fibers (Giraud-Guille et al., 2008), and chitin nanocrystals (Belamie et al., 2004; Revol & Marchessault, 1993). Above a critical concentration C_i, CNCs self-organize to form a biphasic suspension composed of an isotropic upper part, and an anisotropic lower part containing a chiral nematic (or cholesteric) liquid crystalline phase (Revol et al., 1992; Schütz et al., 2015; Ureña-Benavides et al., 2011). The volume fraction of the anisotropic (cholesteric) phase increases with the CNC concentration up to a limit concentration C_a, where all the CNCs

* Corresponding author.
E-mail address: frederic.pignon@univ-grenoble-alpes.fr (F. Pignon).

https://doi.org/10.1016/j.carbpol.2024.122162
Received 23 January 2024; Received in revised form 15 March 2024; Accepted 11 April 2024
Available online 12 April 2024

are in the anisotropic phase.

Various methods can be used to control the orientation of the nanoparticles and obtain functional final properties in the processed material (anisotropic reinforcement, optical properties, controlled porosity): electric and magnetic fields (Cao et al., 2019; Frka-Petesic et al., 2017; Kalidindi et al., 2010; Kvien & Oksman, 2007; Mashkour et al., 2014; Peng et al., 2020), spin-coating (Cranston & Gray, 2006, 2008; Merindol et al., 2020), freeze casting/ice templating (Deville, 2010; Mandin et al., 2021; Munier et al., 2016; Wegst et al., 2010), flow-through (Gevorkian et al., 2021; Hausmann et al., 2018; Nuruddin et al., 2021; Reising et al., 2012) and membrane separation (Chen et al., 2014; Jin et al., 2014, 2015; Metilli et al., 2023; Mianehrow et al., 2020; Rey, Hengl, Baup, Karrouch, Dufresne, et al., 2019; Rey, Hengl, Baup, Karrouch, Gicquel, et al., 2019; Semeraro et al., 2020).

Membrane separation processes possess the advantage of starting from diluted particle suspensions, where the colloidal interactions can be overcome by imposed shear and pressure forces and induce highly concentrated and oriented nanoparticles at the membrane surface. This approach avoids the issues stemming from concentrated suspensions, which exhibit high viscosity and heterogeneous particle dispersion, and are therefore challenging to process in a controlled fashion. Previous works demonstrated the efficiency of membrane separation and drying to produce CNC-based nanocomposites with a uniform layered organization, from nanometers to tens of micrometers (Semeraro et al., 2020). However, a previous work showed that partial relaxation phenomena can occur at the end of filtration when the pressure is released, leading to a loss of organization and orientation (Rey, Hengl, Baup, Karrouch, Dufresne, et al., 2019; Rey, Hengl, Baup, Karrouch, Gicquel, et al., 2019). The preservation of the structure after filtration is therefore critical to the success of this process for the fabrication of novel, attractive biobased materials. In this work, we propose the use of *in situ* UV-curing at the end of the membrane separation process (under maintained constant transmembrane pressure or after a certain relaxation time) to fix the structural organization and orientation reached during the filtration and then after a specific relaxation time.

Several works have attempted to fix CNC structures by UV photopolymerization, such as the cholesteric arrangement for photonic applications (diffraction gratings) (Cao et al., 2020), photonic films used as sensors and anti-counterfeiting labels (Huang et al., 2020; Wu et al., 2016), scaffolds for tissue engineering (Frost et al., 2019) or fabrication of hydrogel fibers (Hou et al., 2017). However, few studies have combined filtration and photopolymerization of CNC suspensions. Amongst these, Wang and coworkers investigated a CNC-polyacrylamide hydrogel formed by filtration and subsequent photopolymerization (Wang et al., 2020). Owing to the fixation of the structure achieved during filtration, they demonstrated the formation of a concentrated layer of cholesteric structures close to the membrane. However, the structural characterization of the concentrated deposit was limited to optical and electron microscopy observations.

In the present study, CNCs were mixed with a poly(ethylene glycol) diacrylate polymer (PEGDA) as a photocurable polymer. The CNC/PEGDA suspensions were fixed by UV radiation either under pressure after a filtration time t_f, or upon releasing the transmembrane pressure (relaxation step) for a time t_r. Different t_f and t_r times were explored to investigate the dynamics of CNC structuration occurring during filtration or upon relaxation. The filtrated and UV-cured PEGDA/CNC deposits were investigated at the nanometric scale with small-angle X-ray scattering (SAXS), using a vertically-collimated beam of 25 μm. This analysis was complemented at the micrometric scale by *ex situ* characterization of the nanocomposites by scanning electron microscopy (SEM). By varying the initial CNC concentration, filtration and relaxation time steps, it was possible to link the processing conditions to the observed nano- and microstructure of the resulting deposit.

2. Materials and methods

2.1. Materials

The CNCs were purchased from the UMaine Development Center (University of Maine, USA) as a suspension in water with a stock concentration of 11.5 wt%. This suspension was sonicated to separate the CNC aggregates (Branson Digital sonifier at 15.47 $kJ.g^{-1}.L^{-1}$). The 11.5 wt% sonicated suspensions were diluted with ultrapure water. The dimensions of the CNCs were measured from transmission electron microscopy (TEM) images of negatively stained preparations on a JEOL JEM-2100 Plus microscope operating at 200 kV. The TEM images are available as Supplementary data (Fig. S1). 225 particles were measured from the TEM images using ImageJ software (National Institute of Health, USA). The CNCs had a length of 127.4 ± 34.1 nm and a width of 10.9 ± 2.6 nm, with an aspect ratio of 12.3 ± 4.3 (Fig. S2). The Irgacure 2959 photoinitiator and poly(ethylene) glycol diacrylate (PEGDA) were purchased from Sigma-Aldrich (France). PEGDA with a molar mass Mw = 700 $g.mol^{-1}$ was selected due to its complete miscibility with water (Nam et al., 2018).

2.2. Preparation of PEGDA/CNC suspensions

To prepare the PEGDA/CNC suspensions, the sonicated CNC suspensions were mixed with PEGDA at a 70/30 weight ratio of [pure PEGDA/aqueous CNC suspension] by magnetic stirring at room temperature. This weight ratio was chosen after several tests as a compromise between material shrinkage after drying, and the presence of a sufficient amount of CNCs in the initial aqueous suspension. When present, bubbles were removed by evacuating the mixture at 0.8 bar for 30 min under a vacuum bell jar. Then, 0.5 wt% (given as percentages of the mass of PEGDA) of Irgacure 2959 was added under stirring until dissolution. The final CNC concentrations in the PEGDA/CNC 70/30 suspension were C = 0.7 or 2 wt%, which means that for 100 g of suspension, there were 0.7 g or 2 g of CNCs and 70 g of PEGDA (0.1 mol).

2.3. Fabrication of nanocomposites: filtration and UV-curing

The suspension of PEGDA/CNC 70/30 containing the photo-initiator (Irgacure 2959) was filtered in a custom-made Teflon filtration cell (100 × 8 × 4 mm^3) (Fig. 1) having the same features as the one used in previous works (Jin et al., 2014; Metilli et al., 2023; Rey, Hengl, Baup, Karrouch, Gicquel, et al., 2019; Semeraro et al., 2020). Here, a specific quartz glass window was designed and inserted in the upper part of the filtration cell in order to apply the UV radiation. The suspension was filtered in frontal mode on a 0.2 μm PVDF membrane (Orélis Environnement, France) for different times under a transmembrane pressure ΔP of $1.2.10^5$ Pa. The permeation flux was measured over time by measuring the mass of the permeate with a balance (Precisa 400M, France). After a specific filtration time t_f (and a relaxation time t_r at ΔP = 0 Pa, for the relaxed samples) the feed channel was exposed to UV radiation (λ = 250–450 nm) for 50 s with a UV lamp (Omnicure S2000, France). The UV-curing treatment was performed through the top quartz window of the filtration cell, penetrating the whole height of the channel and diffusing on the sides for 2 cm. Finally, a solid sample was taken out of the filtration cell and air-dried for at least 24 h in a Petri dish (Fig. 1).

The influence of different process parameters on the final structure of the nanocomposites was studied. Firstly, two different initial CNC concentrations were tested, C = 0.7 wt% and 2 wt%. Two types of procedures were studied: (i) without any relaxation step: for a suspension containing 2 wt% CNCs, the filtration time t_f, before photopolymerization was varied (2, 4, 24 and 65 h). Then, the deposit was UV-cured under pressure; (ii) with a relaxation step: for the suspension containing 2 wt% CNCs, a transmembrane pressure of ΔP of $1.2 .10^5$ Pa was applied during t_f = 24 h, followed by a relaxation step (ΔP = 0 Pa) during a fixed time, t_r. Afterwards, the UV-curing was performed.

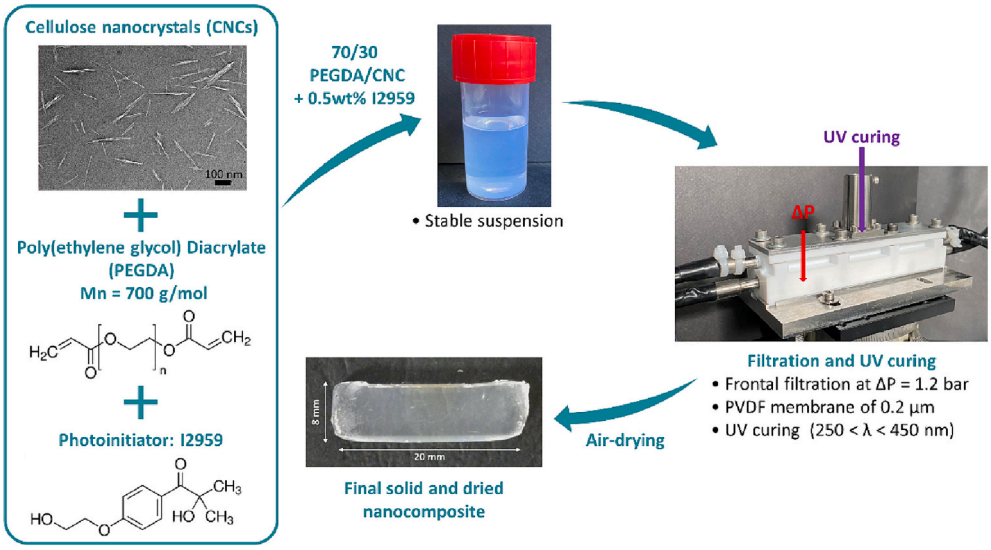

Fig. 1. Flowchart of the nanocomposite manufacturing process. The first step consisted in mixing the PEGDA and CNC suspension in a 70/30 weight ratio. Then the suspension was filtered for various filtration and relaxation times (t_f and t_r). At the end of the process, the suspension was UV-cured. The nanocomposite was then removed from the cell and air-dried.

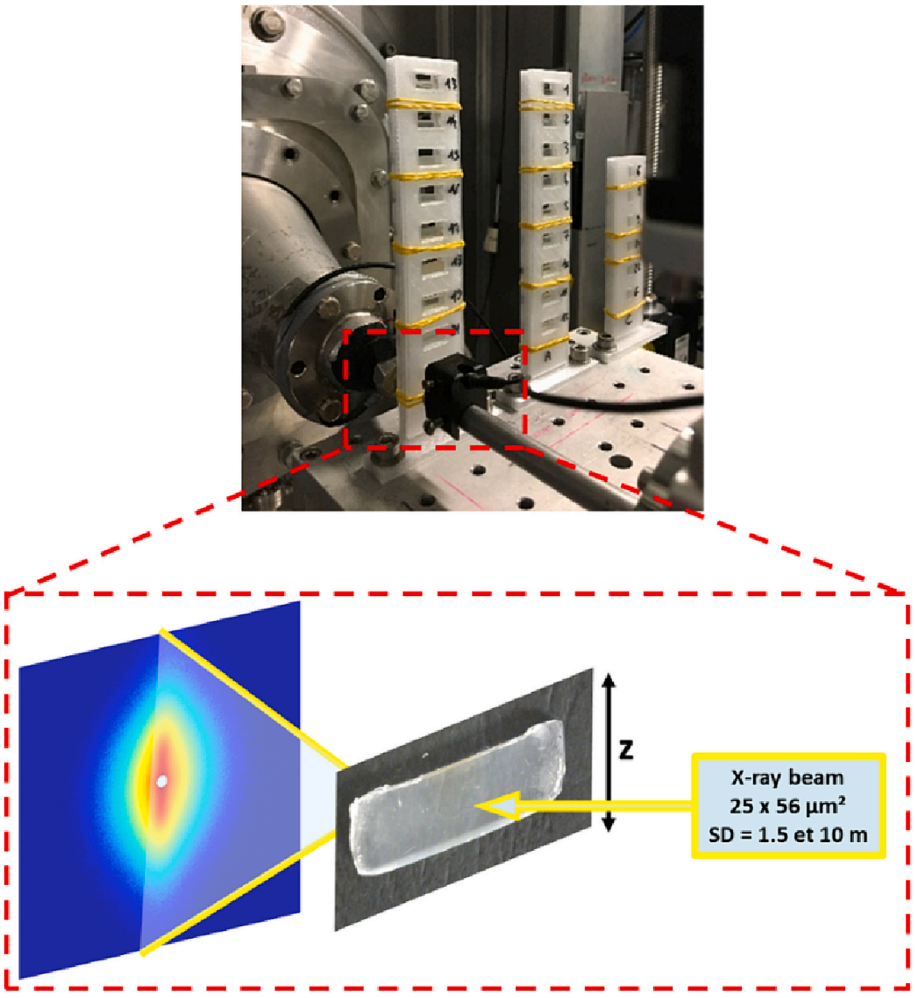

Fig. 2. Photograph of the experimental setup and scheme of the *in-situ* SAXS scanning of the PEGDA/CNC nanocomposites with a 25 µm vertically collimated X-Ray beam.

Different t_r values of 0.5, 2 and 24 h were studied to evaluate their influence on the changes of the structural organization during the relaxation step of the material.

2.4. Small-angle synchrotron X-ray scattering (SAXS)

The SAXS measurements were carried out at the TRUSAXS Instrument of the European Synchrotron Radiation Facility (ESRF) in Grenoble, France (beamline ID02). The measurements were conducted at room temperature, using sample-detector distances of 1.5 and 10 m and 12.232 keV X-ray photons, corresponding to a q-range of 0.02 to 2 nm^{-1}, where $q = (4\pi/\lambda)\sin(\theta/2)$ with θ the scattering angle. A beam with cross-section full-width at half maximum of approximately 25 μm vertically, and 56 μm horizontally at the sample position was obtained using pinhole collimation (Narayanan et al., 2022). The PEGDA/CNC nanocomposites were placed on a sample holder with the vertical direction corresponding to the applied transmembrane pressure, and the incident X-ray beam passed through it along a direction parallel to the membrane surface (Fig. 2). The two-dimensional (2D) scattered intensity patterns were recorded on a high-resolution pixel array detector (EIGER2-4M, Dectris). The measured scattering patterns were normalized to absolute scale following the standard procedure described by Narayanan and coworkers (Narayanan et al., 2022).

During the experiments, the X-ray beam was directed along the x-direction perpendicular to the nanocomposites positioned vertically along the transmembrane pressure direction applied during the filtration process, with dimensions of 20 mm × 6 mm × 3 mm (width × height × thickness). A rotational stage mounted on the sample table was used to align the incident beam parallel to the membrane surface. A vertical translation table was used to probe the structure at different vertical positions z. SAXS patterns were recorded every 25 μm over the entire height of the nanocomposite. The SAXS pattern measured in the concentrated deposit being the most intense was considered as the closest point to the membrane (z_0). Therefore, we defined this z_0 position as the origin at $z = 25$ μm, corresponding to the minimum distance beyond which the SAXS data could be used. A vertical profile was measured for each nanocomposite. The scattered intensity profiles $I(q)$ were then obtained by azimuthally averaging the normalized 2D scattering patterns. The azimuthal averages of the scattering patterns were calculated after patching the gaps between the detector modules using the SAXSUtilities software (Sztucki, 2021). Annular averages were also calculated using the SAXSUtilities software over a q-range from 0.34 to 0.40 nm^{-1}. The scattering intensity as a function of the azimuthal scattering angle ψ in the plane of the 2D SAXS patterns was defined to quantify the degree of orientation as well as its angular variation. The anisotropy analysis was performed from the 2D patterns using the MATLAB-based Small-Angle Scattering Evaluation Tool (SASET) software (Muthig et al., 2013). Specifically, the model-free principal component analysis (PCA) method was chosen, which provides values for the anisotropy ranging from 0 for isotropic suspensions to 1 for fully aligned systems, which is, depending on the system, quantitatively comparable to the commonly used order parameter (Muthig et al., 2013). The anisotropy and the direction of maximum scattering ψ_0 were calculated *via* PCA in the 0.13–1.71 nm^{-1} q-ranges. The relative effect of ultrafiltration on the degree of anisotropy referred to as PCA anisotropy and on the orientation [maximum scattering direction (ψ_0)] of the CNCs after filtration/relaxation/UV-curing processing was quantified as a function of time t_f or t_r and distance z from the membrane surface by these calculations.

In order to measure the average interparticle distance, d, between CNCs as a function of the distance, z, from the membrane surface, z_0, a Kratky plot (corresponding to $q^2.[I(q)]$ *vs.* q) analysis was performed. This has already been measured in several articles (Rey, Hengl, Baup, Karrouch, Dufresne, et al., 2019; Rey, Hengl, Baup, Karrouch, Gicquel, et al., 2019; Schütz et al., 2015) with the following equation:

$$d = 2\pi/q_{peak} \quad (1)$$

where q_{peak} is the position of the maximum scattered intensity.

The average interparticle distance can be related to the CNC concentration. At increasing CNC concentration, one could expect a decrease of interparticle distance as evidenced on static capillary measurements of CNC suspensions already used in previous works (Rey, Hengl, Baup, Karrouch, Gicquel, et al., 2019, Semeraro et al., 2020, Pignon et al., 2021). This analysis allowed determining the interparticle distance profiles in the photopolymerized nanocomposite.

2.5. Scanning electron microscopy (SEM)

The nanocomposites were sectioned at room temperature. The fragments were attached to metallic stubs covered with carbon tape and covered with Au/Pd using a Baltec MED 020 sputter-coater. The fracture surfaces were observed in secondary electron mode with a FEI Quanta-FEG 250 microscope equipped with a field-emission gun and operating at an accelerating voltage of 2.5 kV. The pitch of the cholesteric structures was measured from the SEM images using ImageJ software.

3. Results

3.1. Nanocomposite at C_{CNC} = 2 wt% filtrated for 24 h

During the ultrafiltration of PEGDA/CNC suspensions, the accumulation of nanoparticles on the membrane surface resulted in the formation of the so-called concentration polarization layer (CPL). This particle accumulation induced a decrease of the permeation flow (Fig. S3A) without causing filtration to completely stop, as the filtered mass continued to increase with filtration time (Fig. S3B). By modifying the filtration parameters, the CPL and the structure of these deposits could be controlled. Concentrated deposits were elaborated and organized on a wide range of scales, from nm to μm, starting from a dilute particle suspension. This concentrated deposit was materialized by a white, membrane-like layer at the bottom of the nanocomposite (Fig. 3A). The organization and average distance between CNCs as a function of the height z in the nanocomposite were obtained by raster-scanning the sample during SAXS experiments. The 2D scattering spectra of a 70/30 PEGDA/CNC suspension at an initial concentration of 2 wt%, filtered for 24 h and then photopolymerized are shown in Fig. 3B.

The SAXS patterns were anisotropic, up to a distance of 300 μm, indicating an organization of the CNCs parallel to the membrane surface as already demonstrated using tangential ultrafiltration (Jin et al., 2014; Rey, Hengl, Baup, Karrouch, Gicquel, et al., 2019; Semeraro et al., 2020). Above 300 μm, the scattered signal intensity decreased, and the 2D patterns became circular, corresponding to an isotropic organization (Fig. 3). In addition, the intensity of the scattered signal related to particle concentration decreased with increasing distance from the membrane surface. This distribution reflects a gradient of CNC concentration from the membrane surface to the bulk, associated with the phenomenon of the CPL by formation of a deposit in specific filtration conditions (Bacchin et al., 1995, 2002; Bhattacharjee et al., 1999; Pignon et al., 2012; Semeraro et al., 2020). These results demonstrate the efficiency of this novel approach for designing cellulose nanocomposites by coupling front-end ultrafiltration and *in-situ* UV cross-linking. They also show for the first time that *in-situ* UV cross-linking can preserve the structure achieved by filtration under the imposed experimental conditions.

From the SAXS data, the radial integration of the scattered intensity was deduced as a function of the scattering vector (Fig. S4). Kratky plots of this integration corresponding to $q^2.I(q)$ *vs.* q were drawn for each distance z from the membrane surface (Fig. 4). The intensity of the peak corresponding to the average interparticle distance increased with decreasing distance from the membrane surface, and shifted towards

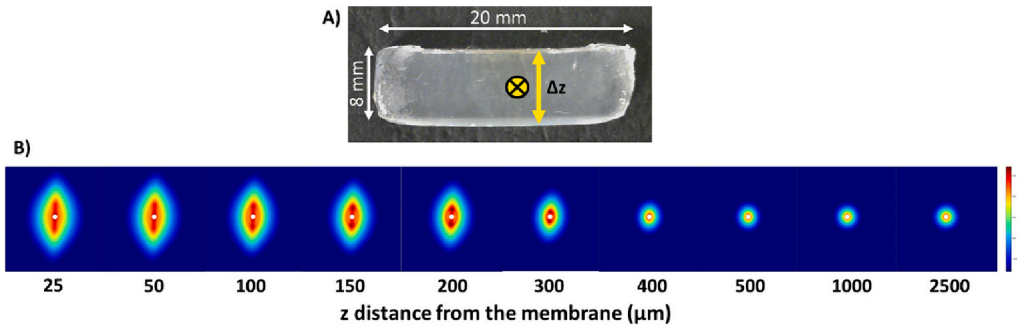

Fig. 3. A) The 70/30 PEGDA/CNC nanocomposite at 2 wt% filtered $t_f = 24$ h and B) the 2D SAXS patterns as a function of distance from the membrane of the nanocomposite.

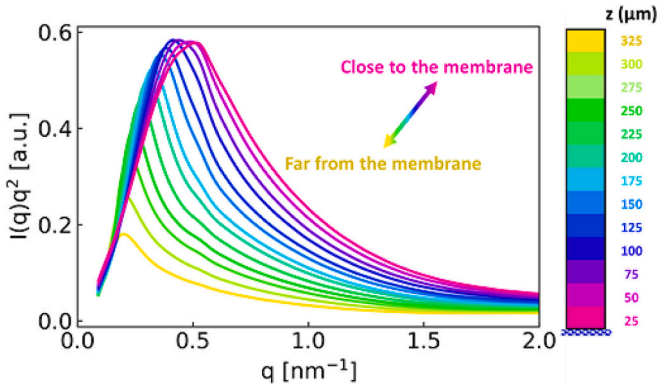

Fig. 4. Kratky plot of the 70/30 PEGDA/CNC nanocomposite at $C_{CNC} = 2$ wt% filtered during $t_f = 24$ h at $\Delta P = 1.2.10^5$ Pa. The colour scale corresponds to the different distances from the membrane.

larger scattering vectors. These two observations indicate the presence of a gradient of interparticle distance within the concentrated deposit and, consequently, a gradient of concentration within the deposit.

By recovering the wave vectors corresponding to each peak of scattered intensity, the average interparticle distance of the CNCs within the concentrated deposit was calculated using Eq. (1). Furthermore, with the PCA analysis of the SAXS patterns (*cf.* Section 3.4), the degree of particle orientation was determined as a function of the distance from the membrane surface. Fig. 5 shows the distribution of average interparticle distance and orientation degree (anisotropy) of CNCs within the concentrated deposit for the 70/30 PEGDA/CNC nanocomposite at C_{CNC}

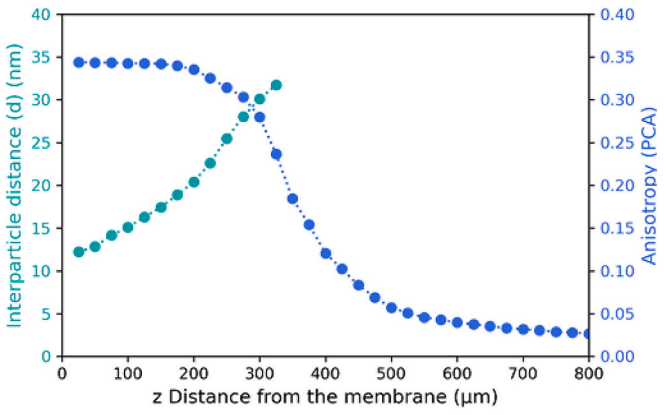

Fig. 5. Variation of the average interparticle distance profile (green) and anisotropy degree (blue) of the CNCs in the concentrated deposit of the 70/30 PEGDA/CNC nanocomposite at $C_{CNC} = 2$ wt% filtered during $t_f = 24$ h at $\Delta P = 1.2 .10^5$ Pa.

= 2 wt% filtered for 24 h.

An interparticle distance of 12 nm was measured in the vicinity of the membrane surface, which increased almost continuously until it reached a value of 31.7 nm at $z = 325$ μm. These distances are significantly smaller than the length of the CNCs (around 130 nm), and close to the smallest width of the CNCs (around 11 nm), showing that the CNCs were highly concentrated and could only be oriented parallel to each other within this thickness of deposit. Beyond this distance, the intensity peak of the scattering patterns corresponding to the average interparticle distance disappeared, due to the predominance of the PEGDA signal at low CNC concentration. This interparticle distance gradient again confirmed the presence of a concentration gradient, with a very high concentration close to the membrane corresponding to $d = 12$ nm under the effect of filtration pressure forces. This underlines one of the advantages of filtration, namely the ability to strongly confine objects from a dilute phase, thus achieving very high concentrations and anisotropy otherwise not achievable if starting from a concentrated suspension.

In addition, the calculation of the anisotropy parameter (PCA) was carried out from the scattering pattern shown in Fig. 3. The degree of anisotropy is presented in Fig. 5 and shows that the anisotropy remained high and constant over a large part of the deposit (around 250–300 μm) at a value of 0.35. It then decreased continuously until it reached a minimum value of 0.02 corresponding to the exit of the CPL, *i.e.* to the initial dilute suspension with an isotropic organization. The application of a pressure field in the vicinity of the membrane resulted in a particle orientation that remained homogeneous over a large region of the deposit. The CPL induced by the accumulation of CNCs on the membrane surface resulted in the formation of anisotropic, structured concentrated layers that could impart specific properties to nanocomposites. However, the layer remained thin and, by adjusting the filtration parameters governing the CPL, it might be possible to modify its organization and structure.

3.2. *Structural control of the orientated layer with the initial CNC concentration in the nanocomposite*

The initial concentration of the suspension is a parameter influencing the final structure of the deposit formed during filtration. Fig. 6A shows the variation in average interparticle distance profiles d for two initial CNC concentrations (0.7 and 2.0 wt%), while Fig. 6B shows the degree of anisotropy as a function of distance from the membrane.

Starting from a lower initial concentration (0.7 wt% compared with 2 wt%), the particle accumulation under the same transmembrane pressure induced the formation of a thinner and slightly less anisotropic layer, but reaching comparable interparticle distances d (13. 4 nm for 0.7 wt% and 12.2 nm for 2 wt%) at $z = 25$ μm, then slightly larger at $z = 225$ μm, with $d = 28.3$ nm for 0.7 wt% *vs.* 22.6 nm for $d = 2$ wt% (Fig. 6A). Starting from a higher concentration, hence more particles, would induce a faster deposit formation and result in a higher densification of the deposit. This explains the tendency for the thickness and

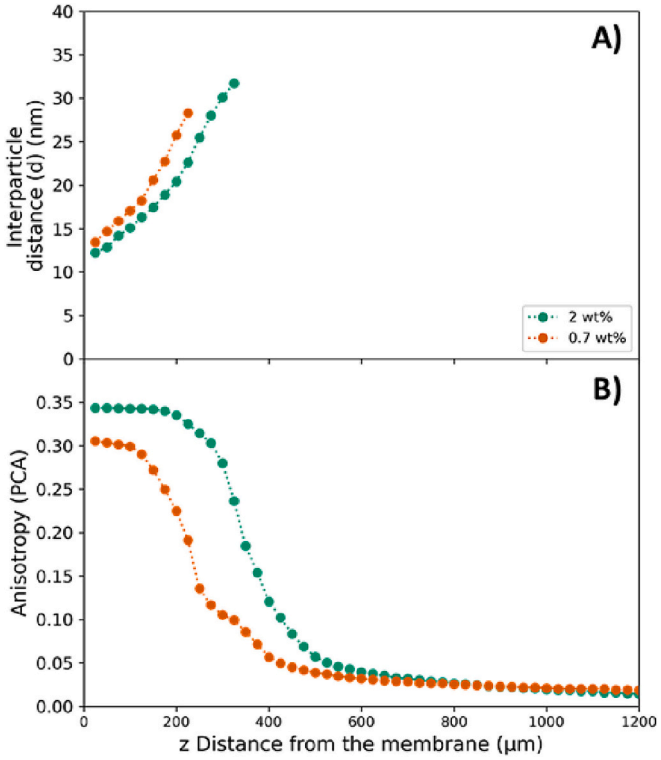

Fig. 6. Influence of the initial CNC concentration on average interparticle distance profiles (A) and nanoparticle orientation (B) in concentrated deposition of 70/30 PEGDA/CNC nanocomposite filtered during $t_f = 24$ h at $\Delta P = 1.2 .10^5$ Pa.

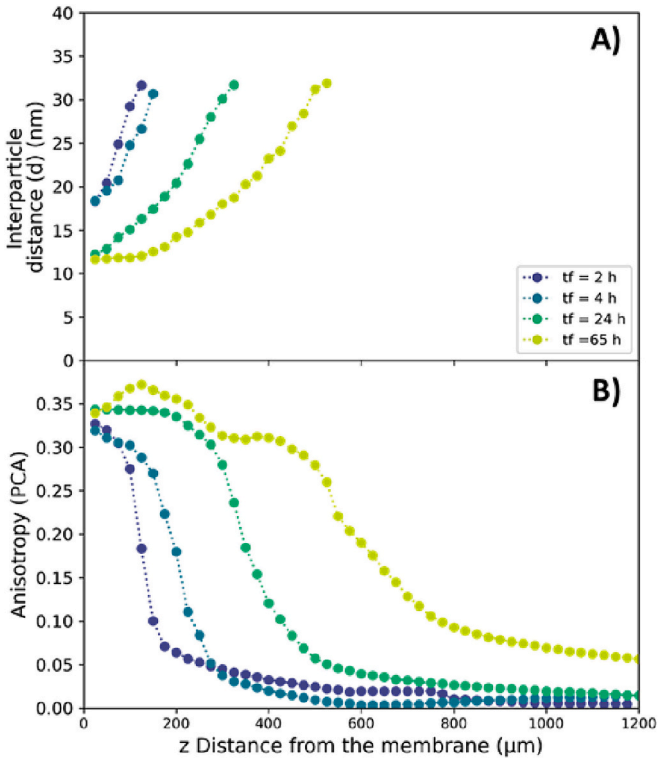

Fig. 7. Influence of filtration time on the distribution (A) and orientation (B) of CNCs in the concentrated deposit of the 70/30 PEGDA/CNC nanocomposite at 2 wt% filtered during $t_f = 24$ h at $\Delta P = 1.2 .10^5$ Pa.

density of the concentrated deposit to increase with increasing initial concentration.

The CNC concentration also influenced the degree of anisotropy near the membrane surface, as shown in Fig. 6B. As previously observed in Fig. 7B, the degree of anisotropy remained high and constant over a large region of the deposits, but with different PCA values depending on the initial concentration of the filtered suspension. A value of 0.35 was found for the suspension at 2 wt% *vs.* 0.30 at 0.7 wt%. This difference can be explained by the fact that a higher initial concentration induces a smaller interparticle distance between the CNCs, which tends to force the CNCs to orient parallel to the membrane surface. Finally, far from the membrane surface, the PCA decreased steadily until it reached a PCA close to 0, corresponding to the exit of the concentration polarization layers for both concentrations (Fig. 6B).

3.3. *Structural control of the oriented layer with filtration time in the nanocomposite*

Fig. 7A shows the average interparticle distance profiles of CNCs in concentrated deposits from the membrane surface ($z = 25$ µm) as a function of filtration time, t_f. A 2 wt% CNC suspension with PEGDA (70/30 mass ratio) was filtered for different times $t_f = 2$, 4, 24, and 65 h, then photopolymerized after each imposed filtration time. Each nanocomposite was then air-dried in a covered Petri dish. These results show the *in-situ* evolution of the structure in the cellulosic materials during elaboration.

Fig. 7B shows that, as the filtration time increased, the concentrated layer thickness increased from 84 µm for 2 h filtration to 464 µm for 65 h filtration. These concentrated layer thickness measurements were carried out using the method described in Fig. S5. This increase in size with filtration time was due to the accumulation of material in the vicinity of the membrane surface during frontal filtration. After 2 h (Fig. 7A), an average interparticle distance d of 18 nm was reached in the vicinity of the membrane at $z = 25$ µm. Over time, this distance evolved very slowly, stabilizing at 12 nm after 65 h of frontal filtration at $z = 25$ µm. The shaping properties of this new process are therefore strongly linked to the filtration performance. This observation was corroborated by the interparticle distance profiles that evolved over time. In cross-flow filtration processes, the increase in thickness of the concentrated layer is governed by the velocity gradient in the vicinity of the membrane surface. Rey et al. showed that the decrease in permeation flux over time under a given transmembrane pressure, and cross-flow rate was not related to the increase in thickness of the concentrated layer but to the CNC concentration at the membrane surface (Rey, Hengl, Baup, Karrouch, Dufresne, et al., 2019; Rey, Hengl, Baup, Karrouch, Gicquel, et al., 2019). In our front-end process, particles accumulated over time, leading to an increase in both concentration and accumulated layer, as shown in Fig. 7A. The filtration time is therefore an important parameter to consider when optimizing and designing structured materials.

As the CNCs got very close to each other in the concentrated deposit, the scattering pattern and the measurement of PCA in the deposits (Fig. 7B) and the orientation of the intensity in 2D SAXS pattern (Fig. 3B) confirmed the presence of an organized structure of CNCs oriented parallel to the membrane surface. A plateau of anisotropy around 0.35, comparable for any filtration time, was present over a large region of the CPL corresponding to the region of the deposit where the average interparticle distance could be measured. After the plateau, the degree of anisotropy decreased continuously until it reached a value close to 0, corresponding to the end of the CPL. These results show that the filtration process was highly effective in orienting the particles, since after 2 h of filtration, the anisotropy degree was already almost the same to within 96.4 % of that at 65 h in the vicinity of the membrane. However, the distance over which the layer exhibited this degree of anisotropy depended on the filtration time, and therefore on the amount of CNCs accumulated on the membrane surface.

These latest results therefore confirmed that, by modifying the

filtration time, the thickness and density of concentrated deposits can be controlled, while maintaining a high degree of particle orientation over a large region of the deposit.

3.4. Structural control of the oriented layer with the relaxation time t_r in the nanocomposites

The final structure of the concentrated deposits was also controlled by modifying the relaxation time t_r corresponding to the cessation of transmembrane pressure ($\Delta P = 0$ Pa). Fig. 8A shows the CNC average interparticle distance profiles in nanocomposites from the membrane surface ($z = 25$ μm) for relaxation times t_r of 0, 2, and 24 h following the filtration of a 2 wt% CNC suspension for $t_f = 24$ h for each experiment.

These results show that, for the first time, PEGDA/CNC nanocomposites formed *in-situ* were successfully polymerized at different relaxation times reaching different structure organizations within the CPL. These snapshots of the relaxed deposits indicate that the cessation of transmembrane pressure resulted in an expansion of the concentrated layers and hence an increase in their thickness. Indeed, the thickness of the concentrated layer was 263 μm at $t_r = 0$, 498 μm at $t_r = 2$ h, and 1436 μm at $t_r = 24$ h (Fig. 8B). These results demonstrate the importance of adapting the relaxation time to control the thickness of oriented and concentrated layers in the nanocomposites. These measurements also revealed that the interparticle distance profiles were prone to homogenization in the CPL with relaxation time.

It can also be noted that near the membrane surface, the interparticle distance increased and therefore concentration values decreased with relaxation time, increasing from $d = 12$ nm under pressure to $d = 22$ nm for the relaxed profile $t_r = 24$ h (Fig. 8A). This shows that relaxation, inducing an increase in deposit thickness, also caused a local decrease in concentration degree in the vicinity of the membrane. Smaller interparticle distances were also measured far from the membrane surface for longer relaxation times. This shows that the CPLs organized under filtration diffused throughout the volume during relaxation while maintaining the organization and distribution of the CNCs.

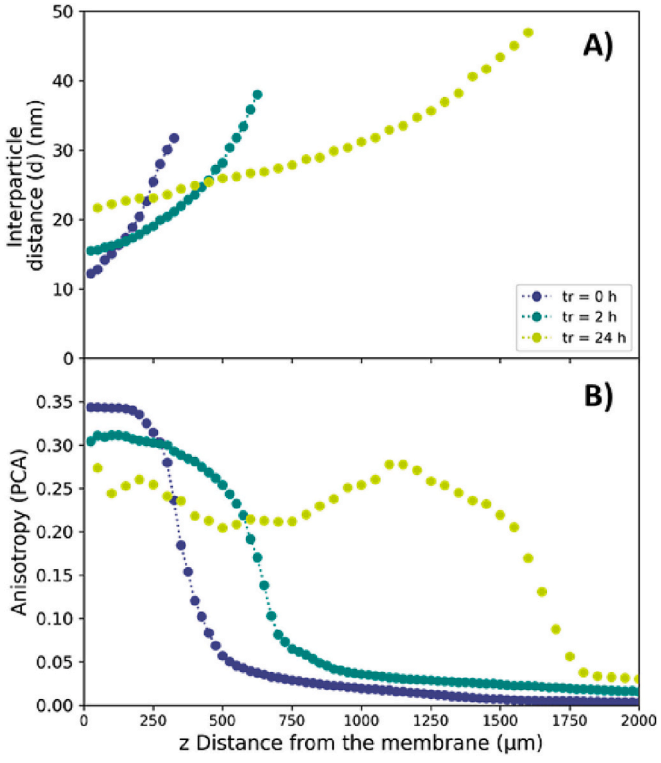

Fig. 8. Influence of relaxation time t_r on the distribution (A) and orientation (B) of CNCs in the concentrated deposition of 2 wt% 70/30 PEGDA/CNC nanocomposite filtered during $t_f = 24$ h at $\Delta P = 1.2 .10^5$ Pa.

This increase in the thickness of the concentrated deposit and the homogenization of the interparticle distance with relaxation time can be explained by the presence of colloidal forces and osmotic pressure, which push the CNCs to diffuse throughout the filtration cell until they reach a state of equilibrium. Moreover, the presence of a large amount of PEGDA significantly increased the viscosity of the suspension, which should slow down the CNC diffusion during relaxation.

The degree of anisotropy (PCA) was plotted as a function of distance from the membrane (Fig. 8B). The anisotropy degree decreased with increasing relaxation time from 0.35 under pressure to 0.25 for $t_r = 24$ h (Fig. 8B). Despite the increase in relaxation time and a decrease in concentration over time, the concentrated deposit remained oriented over a large part of the deposit with still significant anisotropy, *e.g.* with a degree in the 0.2–0.25 range over a distance of ~1.7 μm for $t_r = 24$ h. For the elaboration of nanocomposites with a controlled structure in terms of orientation and thickness, the relaxation time of the deposits is an important parameter to consider.

4. SEM characterization

The SEM images of fractured samples illustrate the efficiency of the membrane separation process (Fig. 9). In the unfiltered 70/30 wt% PEGDA/CNC nanocomposite at 2 wt%, the structure was homogeneous with no defined organization (Fig. 9A). However, the filtered nanocomposite for $t_f = 24$ h contained a layered structure (Fig. 9B). This clearly indicates that the pressure field applied during filtration significantly promoted the texturing of the deposit. The same organization in the form of a well-defined layered structure has been reported by Semeraro et al. for tangential filtration followed by drying of an aqueous CNC suspension (Semeraro et al., 2020). Fig. 10A and B is SEM images of the cross-section of the concentration polarization layer in a 70/30 wt% PEGDA/CNC nanocomposite at $C_{CNC} = 0.7$ wt%, filtered for 24 h. They confirm the SAXS results, highlighting the presence of a homogeneously textured 120-μm-thick deposit. A textured structure is observed in the form of bands oriented parallel to the membrane surface (Fig. 10A), in agreement with the PCA values that suggested a high orientation degree of the particles close to the membrane surface. The high-magnification image in Fig. 10B shows that the bands are indeed arches, corresponding to the section of a cholesteric organization or CNC helicoids, in agreement with the seminal works of Bouligand (Bouligand, 1972, 2008) and reported in another study (Majoinen et al., 2012). Indeed, the filtration of PEGDA/CNC suspensions resulted in the formation of a concentrated deposit in which the CNCs were organized in a cholesteric phase, a structure that could subsequently be fixed by UV polymerization.

The presence of the cholesteric structure can be explained by the fact that close to the membrane surface, a very high concentration was reached with very close particles, forcing CNCs to form cholesteric helicoids, in the presence of PEGDA polymer chains. Moreover, filtration allowed the cholesteric structure to orient, since all the arches observed in the SEM images are oriented parallel to the membrane, which means that the helicoid axes are oriented perpendicular to it. Therefore, in the presence of the photocurable polymer, CNCs are capable of forming an anisotropic cholesteric phase, which was preserved upon UV-curing.

The SEM image in Fig. 10A shows bands with a spacing gradient corresponding to a pitch gradient of the cholesteric organization. Close to the membrane, the interparticle distance is small, leading to very narrow bands. Then, moving away from the membrane surface, this distance increases, as evidenced by increasingly large band spacings. As indicated above, the spacing between the bands gives a fingerprint structure, corresponding to the pitch of the cholesteric structure defined by a 360° rotation of the particles along its helical axis, as explained by Bouligand for biological materials (Bouligand, 1972). In this way, the pitch of the cholesteric structure of the CNC can be measured. From Fig. 10A, the pitch was measured by image analysis, and plotted as a

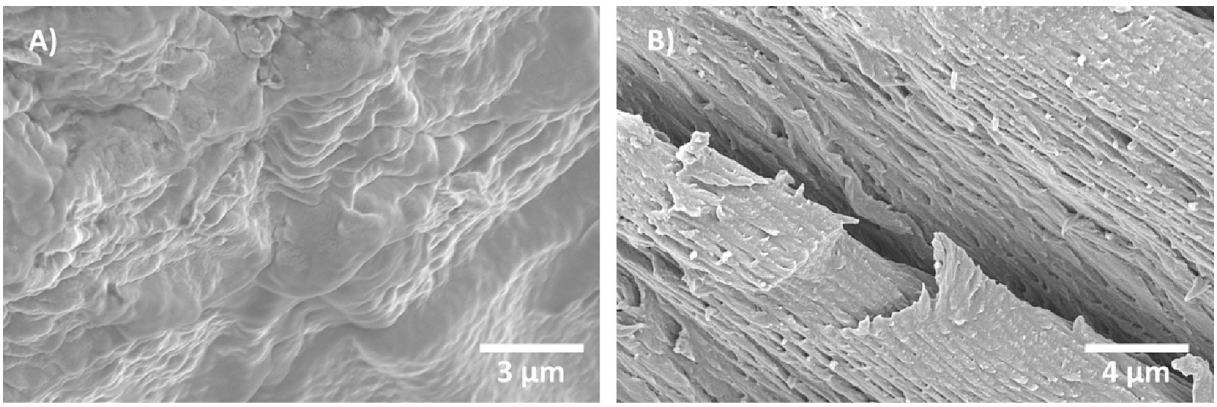

Fig. 9. SEM images of 70/30 wt% PEGDA/CNC nanocomposites at 2 wt%: A) unfiltered B) filtered during $t_f = 24$ h.

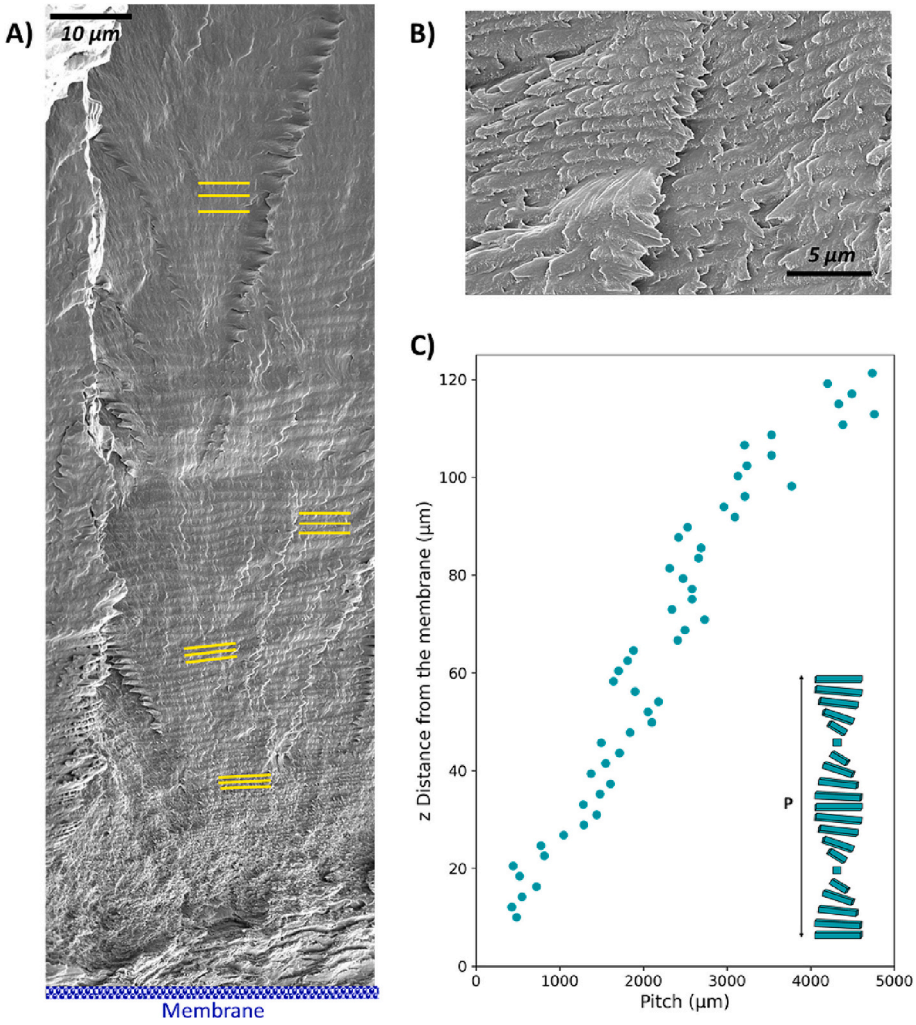

Fig. 10. A) and B) SEM images of a 70/30 wt% PEGDA/CNC nanocomposite at 0.7 wt% obtained by filtration during $t_f = 24$ h at $\Delta P = 1.2 .10^5$ Pa. C) Pitch of cholesteric structures as a function of the distance from the membrane measured from image A. The yellow lines highlight the band spacing (or half-pitch). The image in A is a composite of several aligned images that cover a large surface of the sample while preserving the resolution.

function of distance from the membrane (Fig. 10C). In a recent work describing the structure and transformation of CNC tactoids in a UV-curable polymer matrix, (Wang et al., 2016) observed similar periodic bands, well described from SEM images. The authors produced a deposit with a single period spacing, corresponding to a constant pitch value. In our work, instead, a continuously varying pitch was produced owing to the concentration gradient of the CPL induced by filtration. The pitch increased with increasing distance from the membrane, increasing from around 500 nm at around 20 µm from the membrane surface to 4.5 µm at a distance of 120 µm. The pitch variation as a function of z followed a similar trend for the interparticle distance deduced from SAXS data (Fig. 6). Far away from the membrane surface (typically above 120 µm),

the arches were less clearly defined, suggesting that the cholesteric phase was no longer present and that CNCs were isotropically distributed as the particle concentration decreases and interparticle distance increases. In addition, the SEM observations combined with SAXS data showed that filtration can be used to obtain oriented structures from the nanometer to the micrometer scale.

5. Correlation between SAXS and SEM results

As previously mentioned, variations in interparticle distance were evidenced in the measured profiles, as shown in Fig. 11 (70/30 wt% PEGDA/CNC 0.7 wt% $t_f = 24$ h). At a distance higher than $z = 125$ µm, the interparticle distance did not increase with the same slope as below this value, as was also observed for the 2 wt% sample (Fig. S6). The presence of cholesteric structures in the concentrated deposit observed in SEM improved the understanding of the d (z) and PCA (z) data obtained by SAXS.

It was therefore possible to divide the average interparticle distance and PCA curves obtained by SAXS into 3 main regions (Fig. 11A). The region from 25 to 125 µm, corresponding to the bands closest to the membrane surface, displays the presence of a constant anisotropy at a value of around 0.3, associated with an interparticle distance profile increasing with z (CNC concentration gradient). It should also be noted that the end of the constant anisotropy correlates with the change in slope observed in the interparticle distance profile. To explain this phenomenon of saturated anisotropy, we postulate that CNCs are only organized in a cholesteric structure in the deposit near the membrane surface until a critical interparticle distance, corresponding to the change in slope (P1 and P2 in Fig. 11). This critical interparticle distance value (around 18 nm), is found in the various filtration cases, for the 0.7 and 2 wt% nanocomposites with $t_f = 24$ h (Fig. S6). This cholesteric organization implies a rotation of the CNCs around their cholesteric helical axis, which induces a variation in the orientation angle of the CNCs over distances of the order of a few micrometers (corresponding to the pitch of this organization). This rotation of the CNCs around their cholesteric helical axis was observed within the volume determined by the collimation width of the X-ray beam, *i.e.* over 25 × 56 µm. However, in SEM images, all the bands are oriented in the same direction, parallel to the membrane surface, which means that the cholesteric domains are all oriented in the same direction. This justifies why the anisotropy observed in SAXS data is maximal and constant beyond a degree of interparticle distance corresponding to the formation of a cholesteric structure since the observation was made at the scale of the particles, which had different angles of orientation when they were organized in a cholesteric structure. This hypothesis was supported by the measurements from SEM images, which showed that the cholesteric structure extended for 120 µm, corresponding to the length of the anisotropy plateau observed in the SAXS curves.

In the region extending from 125 to 225 µm (Fig. 11A), corresponding to the region above the critical interparticle distance for cholesteric structure formation (18 nm), extending to the last interparticle distance measurement, the interparticle distance increased with increasing distance from the membrane surface, while the anisotropy decreased. The coexistence of cholesteric and isotropic domains in this transition region could explain these variations (Fig. 11B). This was confirmed by other observations at different length scales. Indeed, this region would correspond to a transition from an isotropic state far from the membrane to an assembly of CNCs in a chiral nematic structure close to the membrane. As the CNCs approach the membrane, the increase in concentration induces a decrease in the interparticle distance, and a compaction of the particle assembly. The steric constraint thus promotes the parallel orientation of CNCs, which explains the increase in

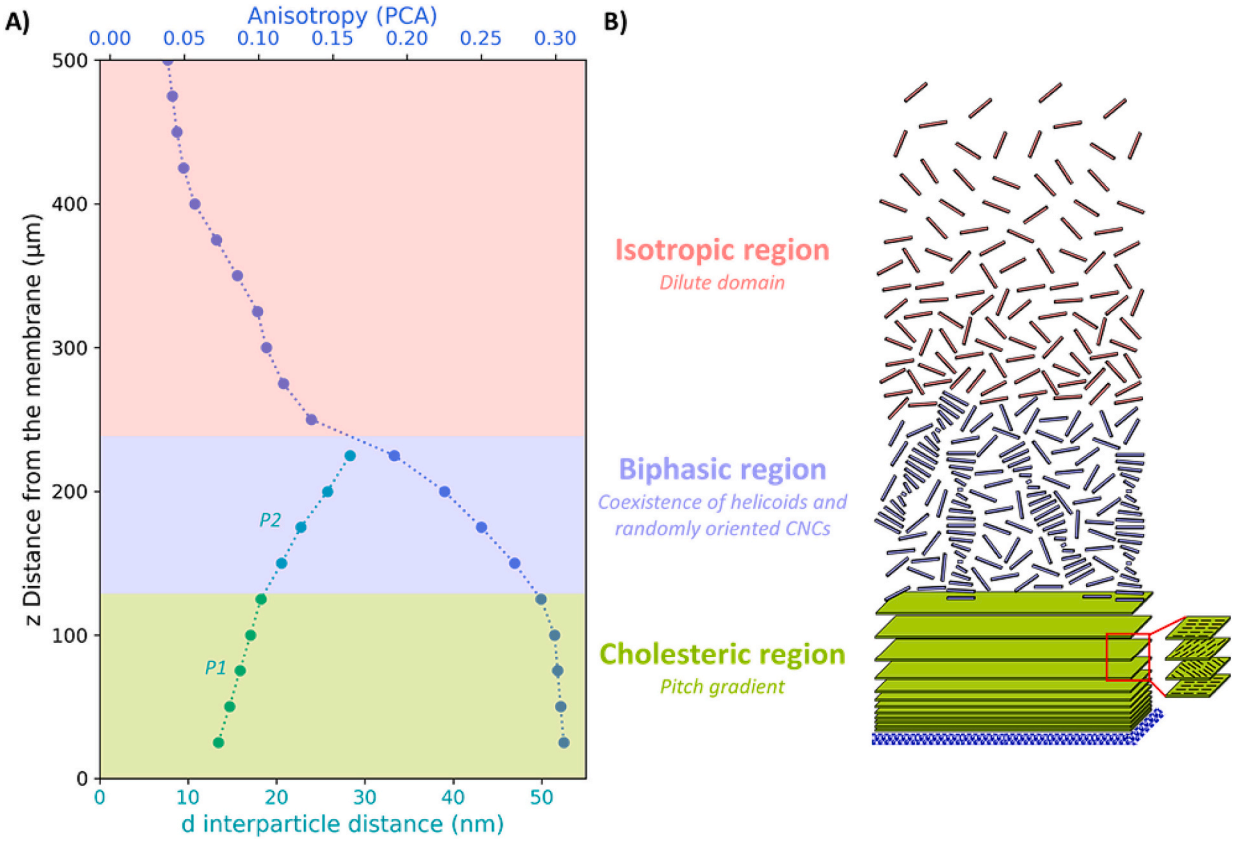

Fig. 11. Variation of the average interparticle distance and PCA degree (A) and schematic CNC organization in the concentrated deposit (B) with 3 regions: (green) cholesteric region with pitch gradient, (purple) biphasic region and (pink) isotropic region. These results corresponding to the 70/30 PEGDA/CNC nanocomposite at 0.7 wt% filtered during 24 h at $\Delta P = 1.2 .10^5$ Pa.

anisotropy.

In the region from 225 to 500 μm (Fig. 11A), the interparticle distance was no longer measurable with the setup used in our study, and the PCA profile decreased, then stabilized close to 0. This means that this region corresponded to an almost isotropic region with a random particle organization (Fig. 11B) and therefore a value of the anisotropy degree decreasing to close to 0.

6. Conclusion

In this study, we demonstrated the efficacy of combining membrane separation and UV curing as a process to manufacture cellulose-based composites, with a controlled structure on length scales ranging from nanometers to micrometers. We have shown from SAXS data that concentrated deposits highly oriented at the nanometric scale could be obtained with CNCs oriented parallel to the membrane surface. SEM images revealed the presence of a cholesteric structure with its helical axis oriented perpendicular to the membrane surface, confirming a micrometer-scale organization. Furthermore, a continuous pitch gradient was measured, with a value evolving from 0.5 to 4.5 μm at a distance of 20 to 120 μm from the membrane surface, respectively. To the best of our knowledge, it is the first time such an organized structure is obtained, paving the way to fabricate in a straightforward manner nanocomposite with cholesteric organizations and continuously varying pitches, with potential applications in photonics.

Moreover, we have proved that the final structure of concentrated deposits could easily be controlled in terms of thickness, distribution, and CNC orientation by tuning the filtration parameters such as the initial suspension concentration, the filtration time, or the relaxation time. The different analysis evidenced that, depending on the applied filtration and relaxation steps, the orientation and structure of the concentrated CNC deposits were successfully frozen after UV-curing. Our results confirmed the colloidal stability and homogeneous organization of the CNCs in the polymer matrix at this 70/30 polymer-to-cnc ratio, inducing a homogeneous structuring at high CNC concentrations reached in the deposits. This point is important in the prospect of constructing homogeneous CNC-based nanocomposites with enhanced mechanical or barrier properties, which are attractive features in industrial applications (packaging, photonic sensors, reinforcement materials).

CRediT authorship contribution statement

S. Mandin: Writing – review & editing, Writing – original draft, Methodology, Investigation, Formal analysis. **L. Metilli:** Writing – review & editing, Investigation, Formal analysis. **M. Karrouch:** Investigation. **C. Lancelon-Pin:** Writing – review & editing, Investigation, Formal analysis. **J.-L. Putaux:** Writing – review & editing, Investigation, Formal analysis. **W. Chèvremont:** Writing – review & editing, Investigation, Formal analysis. **E. Paineau:** Writing – review & editing, Investigation, Formal analysis. **N. Hengl:** Writing – review & editing, Supervision, Investigation, Formal analysis. **B. Jean:** Writing – review & editing, Supervision, Investigation, Formal analysis. **F. Pignon:** Writing – review & editing, Writing – original draft, Supervision, Project administration, Investigation, Funding acquisition, Formal analysis, Conceptualization.

Declaration of competing interest

The authors declare that they have no known competing financial interests or personal relationships that could have appeared to influence the work reported in this paper.

Data availability

Data will be made available on request.

Data from ESRF can be found online at https://doi.esrf.fr/10.15151/ESRF-ES-1030392887.

Acknowledgements

We thank Theyencheri Narayanan (ESRF, Grenoble), Didier Blésès, Frédéric Hugenell and Eric Faivre (Laboratoire Rhéologie et Procédés) for technical assistance. ESRF is acknowledged for the provision of synchrotron beamtime (proposal SC-5319). We thank also Fanny Bosson (Laboratoire Rhéologie et Procédés) and Thomas Gibaud (Laboratoire de Physique ENS de Lyon) for their help during the experiments at ESRF. The authors acknowledge the support of the French Agence Nationale de la Recherche (ANR), under grant agreement #ANR-20-CE43-0015 (ANISOFILM) for financial support of S. Mandin's PhD thesis and L. Metilli's postdoctoral position. The authors would like to thank the NanoBio-ICMG Platform (UAR 2607, Grenoble) for granting access to the electron microscopy facilities. LRP is part of LabEx Tec21 (Investissements d'Avenir - grant agreement #ANR-11-LABX-0030). LRP and CERMAV are part of Institut Carnot PolyNat (Investissements d'Avenir - grant agreement #ANR-16-CARN-0025-01), and the Glyco@Alps programme (Investissements d'Avenir - grant agreement #ANR-15-IDEX-02).

Appendix A. Supplementary data

Supplementary data to this article can be found online at https://doi.org/10.1016/j.carbpol.2024.122162.

References

Bacchin, P., Aimar, P., & Sanchez, V. (1995). Model for colloidal fouling of membranes. *AICHE Journal, 41*(2), 368–376. https://doi.org/10.1002/aic.690410218

Bacchin, P., Si-Hassen, D., Starov, V., Clifton, M. J., & Aimar, P. (2002). A unifying model for concentration polarization, gel-layer formation and particle deposition in cross-flow membrane filtration of colloidal suspensions. *Chemical Engineering Science, 57*(1), 77–91. https://doi.org/10.1016/S0009-2509(01)00316-5

Bawden, F. C., Pirie, N. W., Bernal, J. D., & Fankuchen, I. (1936). Liquid crystalline substances from virus-infected plants. *Nature, 138*, 1051–1052. https://doi.org/10.1038/1381051a0

Belamie, E., Davidson, P., & Giraud-Guille, M. M. (2004). Structure and chirality of the nematic phase in α-chitin suspensions. *The Journal of Physical Chemistry B, 108*(39), 14991–15000. https://doi.org/10.1021/jp048152u

Bhattacharjee, S., Kim, A. S., & Elimelech, M. (1999). Concentration polarization of interacting solute particles in cross-flow membrane filtration. *Journal of Colloid and Interface Science, 212*(1), 81–99. https://doi.org/10.1006/jcis.1998.6045

Bouligand, Y. (1972). Twisted fibrous arrangements in biological materials and cholesteric mesophases. *Tissue and Cell, 4*(2), 189–217. https://doi.org/10.1016/S0040-8166(72)80042-9

Bouligand, Y. (2008). Liquid crystals and biological morphogenesis: Ancient and new questions. *Comptes Rendus Chimie, 11*(3), 281–296. https://doi.org/10.1016/j.crci.2007.10.001

Cao, L., Cheng, Z., Yan, M., & Chen, Y. (2019). Anisotropic rubber nanocomposites via magnetic-induced alignment of Fe3O4/cellulose nanocrystals hybrids obtained by templated assembly. *Chemical Engineering Journal, 363*, 203–212. https://doi.org/10.1016/j.cej.2019.01.126

Cao, Y., Wang, P.-X., D'Acierno, F., Hamad, W. Y., Michal, C. A., & MacLachlan, M. J. (2020). Tunable diffraction gratings from biosourced lyotropic liquid crystals. *Advanced Materials, 32*(19), Article 1907376. https://doi.org/10.1002/adma.201907376

Chen, Q., Liu, P., Nan, F., Zhou, L., & Zhang, J. (2014). Tuning the iridescence of chiral nematic cellulose nanocrystal films with a vacuum-assisted self-assembly technique. *Biomacromolecules, 15*(11), 4343–4350. https://doi.org/10.1021/bm501355x

Cranston, E. D., & Gray, D. G. (2006). Morphological and optical characterization of polyelectrolyte multilayers incorporating nanocrystalline cellulose. *Biomacromolecules, 7*(9), 2522–2530. https://doi.org/10.1021/bm0602886

Cranston, E. D., & Gray, D. G. (2008). Birefringence in spin-coated films containing cellulose nanocrystals. *Colloids and Surfaces A: Physicochemical and Engineering Aspects, 325*(1), 44–51. https://doi.org/10.1016/j.colsurfa.2008.04.042

Davidson, P., & Gabriel, J.-C. P. (2005). Mineral liquid crystals. *Current Opinion in Colloid & Interface Science, 9*(6), 377–383. https://doi.org/10.1016/j.cocis.2004.12.001

Davidson, P., Garreau, A., & Livage, J. (1994). Nematic colloidal suspensions of V2O5 in water—Or Zocher phases revisited. *Liquid Crystals, 16*(5), 905–910. https://doi.org/10.1080/02678299408027861

Deville, S. (2010). Freeze-casting of porous biomaterials: Structure, properties and opportunities. *Materials, 3*(3), Article 3. https://doi.org/10.3390/ma3031913

Dogic, Z., & Fraden, S. (2000). Cholesteric phase in virus suspensions. *Langmuir, 16*(20), 7820–7824. https://doi.org/10.1021/la000446t

Folda, T., Hoffmann, H., Chanzy, H., & Smith, P. (1988). Liquid crystalline suspensions of poly(tetrafluoroethylene) "whiskers". *Nature, 333*(6168), Article 6168. https://doi.org/10.1038/333055a0

Frka-Petesic, B., Guidetti, G., Kamita, G., & Vignolini, S. (2017). Controlling the photonic properties of cholesteric cellulose nanocrystal films with magnets. *Advanced Materials, 29*(32), Article 1701469. https://doi.org/10.1002/adma.201701469

Frost, B. A., Sutliff, B. P., Thayer, P., Bortner, M. J., & Foster, E. J. (2019). Gradient poly (ethylene glycol) diacrylate and cellulose nanocrystals tissue engineering composite scaffolds via extrusion bioprinting. *Frontiers in Bioengineering and Biotechnology, 7*, 280. https://doi.org/10.3389/fbioe.2019.00280

Gevorkian, A., Morozova, S. M., Kheiri, S., Khuu, N., Chen, H., Young, E., … Kumacheva, E. (2021). Actuation of three-dimensional-printed nanocolloidal hydrogel with structural anisotropy. *Advanced Functional Materials, 31*(17), Article 2010743. https://doi.org/10.1002/adfm.202010743

Giraud-Guille, M. M., Mosser, G., & Belamie, E. (2008). Liquid crystallinity in collagen systems in vitro and in vivo. *Current Opinion in Colloid & Interface Science, 13*(4), 303–313. https://doi.org/10.1016/j.cocis.2008.03.002

Grelet, E., & Fraden, S. (2003). What is the origin of chirality in the cholesteric phase of virus suspensions? *Physical Review Letters, 90*(19), Article 198302. https://doi.org/10.1103/PhysRevLett.90.198302

Hausmann, M. K., Rühs, P. A., Siqueira, G., Läuger, J., Libanori, R., Zimmermann, T., & Studart, A. R. (2018). Dynamics of cellulose nanocrystal alignment during 3D printing. *ACS Nano, 12*(7), 6926–6937. https://doi.org/10.1021/acsnano.8b02366

Hou, K., Li, Y., Liu, Y., Zhang, R., Hsiao, B. S., & Zhu, M. (2017). Continuous fabrication of cellulose nanocrystal/poly(ethylene glycol) diacrylate hydrogel fiber from nanocomposite dispersion: Rheology, preparation and characterization. *Polymer, 123*, 55–64. https://doi.org/10.1016/j.polymer.2017.06.034

Huang, Y., Chen, G., Liang, Q., Yang, Z., & Shen, H. (2020). Multifunctional cellulose nanocrystal structural colored film with good flexibility and water-resistance. *International Journal of Biological Macromolecules, 149*, 819–825. https://doi.org/10.1016/j.ijbiomac.2020.01.247

Jin, Y., Hengl, N., Baup, S., Pignon, F., Gondrexon, N., Magnin, A., Sztucki, M., Narayanan, T., Michot, L., & Cabane, B. (2014). Effects of ultrasound on colloidal organization at nanometer length scale during cross-flow ultrafiltration probed by in-situ SAXS. *Journal of Membrane Science, 453*, 624–635. https://doi.org/10.1016/j.memsci.2013.12.001

Jin, Y., Hengl, N., Baup, S., Pignon, F., Gondrexon, N., Sztucki, M., Romdhane, A., Guillet, A., & Aurousseau, M. (2015). Ultrasonic assisted cross-flow ultrafiltration of starch and cellulose nanocrystals suspensions: Characterization at multi-scales. *Carbohydrate Polymers, 124*, 66–76. https://doi.org/10.1016/j.carbpol.2015.01.073

Kalidindi, S., Ounaies, Z., & Kaddami, H. (2010). *Toward the preparation of nanocomposites with oriented fillers: Electric field-manipulation of cellulose whiskers in silicone oil. 19(9)* p. 094002). https://doi.org/10.1088/0964-1726/19/9/094002

Kvien, I., & Oksman, K. (2007). Orientation of cellulose nanowhiskers in polyvinyl alcohol. *Applied Physics A, 87*(4), 641–643. https://doi.org/10.1007/s00339-007-3882-3

Lekkerkerker, H. N. W., & Vroege, G. J. (2013). Liquid crystal phase transitions in suspensions of mineral colloids: New life from old roots. *Philosophical Transactions of the Royal Society A: Mathematical, Physical and Engineering Sciences, 371*(1988), Article 20120263. https://doi.org/10.1098/rsta.2012.0263

Majoinen, J., Kontturi, E., Ikkala, O., & Gray, D. G. (2012). SEM imaging of chiral nematic films cast from cellulose nanocrystal suspensions. *Cellulose, 19*(5), 1599–1605. https://doi.org/10.1007/s10570-012-9733-1

Mandin, S., Moreau, S., Talantikite, M., Novalès, B., Maigret, J.-E., Cathala, B., & Moreau, C. (2021). Cellulose nanofibrils/xyloglucan bio-based aerogels with shape recovery. *Gels, 7*(1), 5. https://doi.org/10.3390/gels7010005

Marchessault, R. H., Morehead, F. F., & Walter, N. M. (1959). Liquid crystal systems from fibrillar polysaccharides. *Nature, 184*(4686), 632–633. https://doi.org/10.1038/184632a0

Mashkour, M., Kimura, T., Kimura, F., Mashkour, M., & Tajvidi, M. (2014). Tunable self-assembly of cellulose nanowhiskers and polyvinyl alcohol chains induced by surface tension torque. *Biomacromolecules, 15*(1), 60–65. https://doi.org/10.1021/bm401287s

Merindol, R., Diabang, S., Mujica, R., Le Houerou, V., Roland, T., Gauthier, C., … Felix, O. (2020). Assembly of anisotropic nanocellulose films stronger than the original tree. *ACS Nano, 14*(12), 16525–16534. https://doi.org/10.1021/acsnano.0c01372

Metilli, L., Ugo, H., Chèvremont, W., Picard, C., & Pignon, F. (2023). Self-supported MOF/cellulose-nanocrystals materials designed from ultrafiltration. *Soft Matter, 19*(42), 8228–8239. https://doi.org/10.1039/D3SM00798G

Mianehrow, H., Re, G. L., Carosio, F., Fina, A., Larsson, P. T., Chen, P., & Berglund, L. A. (2020). Strong reinforcement effects in 2D cellulose nanofibril–graphene oxide (CNF–GO) nanocomposites due to GO-induced CNF ordering. *Journal of Materials Chemistry A, 8*(34), 17608–17620. https://doi.org/10.1039/D0TA04406G

Munier, P., Gordeyeva, K., Bergström, L., & Fall, A. B. (2016). Directional freezing of nanocellulose dispersions aligns the rod-like particles and produces low-density and robust particle networks. *Biomacromolecules, 17*(5), 1875–1881. https://doi.org/10.1021/acs.biomac.6b00304

Muthig, M., Prévost, S., Orglmeister, R., & Gradzielski, M. (2013). SASET: A program for series analysis of small-angle scattering data. *Journal of Applied Crystallography, 46*(4), 1187–1195. https://doi.org/10.1107/S0021889813016658

Nam, C., Yoon, J., Ryu, S. A., Choi, C.-H., & Lee, H. (2018). Water and oil insoluble PEGDA-based microcapsule: Biocompatible and multicomponent encapsulation. *ACS Applied Materials & Interfaces, 10*(47), 40366–40371. https://doi.org/10.1021/acsami.8b16876

Narayanan, T., Sztucki, M., Zinn, T., Kieffer, J., Homs-Puron, A., Gorini, J., Van Vaerenbergh, P., & Boesecke, P. (2022). Performance of the time-resolved ultra-small-angle X-ray scattering beamline with the Extremely Brilliant Source. *Journal of Applied Crystallography, 55*(1), 98–111. https://doi.org/10.1107/S1600576721012693

Nechyporchuk, O., Naceur Belgacem, M., & Bras, J. (2016). Production of cellulose nanofibrils: A review of recent advances. *Industrial Crops and Products, 93*, 2–25. https://doi.org/10.1016/j.indcrop.2016.02.016

Nuruddin, M., Chowdhury, R. A., Szeto, R., Howarter, J. A., Erk, K. A., Szczepanski, C. R., & Youngblood, J. P. (2021). Structure–property relationship of cellulose nanocrystal–polyvinyl alcohol thin films for high barrier coating applications. *ACS Applied Materials & Interfaces, 13*(10), 12472–12482. https://doi.org/10.1021/acsami.0c21525

Peng, N., Huang, D., Gong, C., Wang, Y., Zhou, J., & Chang, C. (2020). Controlled arrangement of nanocellulose in polymeric matrix: From reinforcement to functionality. *ACS Nano, 14*(12), 16169–16179. https://doi.org/10.1021/acsnano.0c08906

Pignon, F., Abyan, M., David, C., Magnin, A., & Sztucki, M. (2012). In situ characterization by SAXS of concentration polarization layers during cross-flow ultrafiltration of laponite dispersions. *Langmuir, 28*(2), 1083–1094. https://doi.org/10.1021/la201492z

Pignon, F., Challamel, M., De Geyer, A., Elchamaa, M., Semeraro, E. F., Hengl, N., , … Bras, J., et al. (2021). Breakdown and buildup mechanisms of cellulose nanocrystal suspensions under shear and upon relaxation probed by SAXS and SALS. *Carbohydr. Polym., 260*, Article 117751.

Reising, A. B., Moon, R. J., & Youngblood, J. P. (2012). Effect of particle alignment on mechanical properties of neat cellulose nanocrystal films. *Journal of Science & Technology for Forest Products and Processes, 2*(6), 32–41.

Revol, J.-F., Bradford, H., Giasson, J., Marchessault, R. H., & Gray, D. G. (1992). Helicoidal self-ordering of cellulose microfibrils in aqueous suspension. *International Journal of Biological Macromolecules, 14*(3), 170–172. https://doi.org/10.1016/S0141-8130(05)80008-X

Revol, J.-F., & Marchessault, R. H. (1993). In vitro chiral nematic ordering of chitin crystallites. *International Journal of Biological Macromolecules, 15*(6), 329–335. https://doi.org/10.1016/0141-8130(93)90049-R

Rey, C., Hengl, N., Baup, S., Karrouch, M., Dufresne, A., Djeridi, H., Dattani, R., & Pignon, F. (2019). Velocity, stress and concentration fields revealed by micro-PIV and SAXS within concentration polarization layers during cross-flow ultrafiltration of colloidal Laponite clay suspensions. *Journal of Membrane Science, 578*, 69–84. https://doi.org/10.1016/j.memsci.2019.02.019

Rey, C., Hengl, N., Baup, S., Karrouch, M., Gicquel, E., Dufresne, A., … Pignon, F. (2019). Structure, rheological behavior, and in situ local flow fields of cellulose nanocrystal dispersions during cross-flow ultrafiltration. *ACS Sustainable Chemistry & Engineering, 7*(12), 10679–10689. https://doi.org/10.1021/acssuschemeng.9b01333

Schütz, C., Agthe, M., Fall, A. B., Gordeyeva, K., Guccini, V., Salajková, M., … Bergström, L. (2015). Rod packing in chiral nematic cellulose nanocrystal dispersions studied by small-angle X-ray scattering and laser diffraction. *Langmuir, 31*(23), 6507–6513. https://doi.org/10.1021/acs.langmuir.5b00924

Semeraro, E. F., Hengl, N., Karrouch, M., Michot, L. J., Paineau, E., Jean, B., … Pignon, F. (2020). Layered organization of anisometric cellulose nanocrystals and beidellite clay particles accumulated near the membrane surface during cross-flow ultrafiltration: In situ SAXS and ex situ SEM/WAXD characterization. *Colloids and Surfaces A: Physicochemical and Engineering Aspects, 584*, Article 124030. https://doi.org/10.1016/j.colsurfa.2019.124030

Strzelecka, T. E., Davidson, M. W., & Rill, R. L. (1988). Multiple liquid crystal phases of DNA at high concentrations. *Nature, 331*, 457–460. https://doi.org/10.1038/331457a0

Sztucki, M. (2021). *SAXSutilities2: A graphical user interface for processing and analysis of Small-Angle X-ray Scattering data [Computer software]*. Zenodo. https://doi.org/10.5281/zenodo.5825707

Ureña-Benavides, E. E., Ao, G., Davis, V. A., & Kitchens, C. L. (2011). Rheology and phase behavior of lyotropic cellulose nanocrystal suspensions. *Macromolecules, 44*(22), 8990–8998. https://doi.org/10.1021/ma201649f

Wang, P.-X., Hamad, W. Y., & MacLachlan, M. J. (2016). Structure and transformation of tactoids in cellulose nanocrystal suspensions. *Nature Communications, 7*, 11515. https://doi.org/10.1038/ncomms11515

Wang, Z., Yuan, Y., Hu, J., Yang, J., Feng, F., Yu, Y., Liu, P., Men, Y., & Zhang, J. (2020). Origin of vacuum-assisted chiral self-assembly of cellulose nanocrystals. *Carbohydrate Polymers, 245*, Article 116459. https://doi.org/10.1016/j.carbpol.2020.116459

Wegst, U. G. K., Schecter, M., Donius, A. E., & Hunger, P. M. (2010). Biomaterials by freeze casting. *Philosophical Transactions of the Royal Society A: Mathematical, Physical and Engineering Sciences, 368*(1917), 2099–2121. https://doi.org/10.1098/rsta.2010.0014

Wu, T., Li, J., Li, J., Ye, S., Wei, J., & Guo, J. (2016). A bio-inspired cellulose nanocrystal-based nanocomposite photonic film with hyper-reflection and humidity-responsive actuator properties. *Journal of Materials Chemistry C, 4*(41), 9687–9696. https://doi.org/10.1039/C6TC02629J

Zocher, H. (1925). Über freiwillige Strukturbildung in Solen. (Eine neue Art anisotrop flüssiger Medien.). *Zeitschrift für Anorganische und Allgemeine Chemie, 147*(1), 91–110. https://doi.org/10.1002/zaac.19251470111